Green's function approximation from cross-correlations of 20–100 Hz noise during a tropical storm

Laura A. Brooks[a] and Peter Gerstoft
Marine Physical Laboratory, Scripps Institution of Oceanography, La Jolla, California 92093

(Received 8 May 2008; revised 2 October 2008; accepted 4 December 2008)

Approximation of Green's functions through cross-correlation of acoustic signals in the ocean, a method referred to as ocean acoustic interferometry, is potentially useful for estimating parameters in the ocean environment. Travel times of the main propagation paths between hydrophone pairs were estimated from interferometry of ocean noise data that were collected on three L-shaped arrays off the New Jersey coast while Tropical Storm Ernesto passed nearby. Examination of the individual noise spectra and their mutual coherence reveals that the coherently propagating noise is dominated by signals of less than 100 Hz. Several time and frequency noise normalization techniques were applied to the low frequency data in order to determine the effectiveness of each technique for ocean acoustic applications. Travel times corresponding to the envelope peaks of the noise cross-correlation time derivatives of data were extracted from all three arrays, and are shown to be in agreement with the expected direct, surface-reflected, and surface-bottom-reflected interarray hydrophone travel times. The extracted Green's function depends on the propagating noise. The Green's function paths that propagate horizontally are extracted from long distance shipping noise, and during the storm the more vertical paths are extracted from breaking waves. *© 2009 Acoustical Society of America.* [DOI: 10.1121/1.3056563]

PACS number(s): 43.30.Pc, 43.60.Fg, 43.30.Nb [RCG] Pages: 723–734

I. INTRODUCTION

In 2001 Lobkis and Weaver[1] showed, both theoretically and experimentally, that the Green's function between two points can be determined from temporal cross-correlation within a diffuse ultrasonic field. Extraction of the Green's function by cross-correlation has since been applied to numerous areas including ultrasonics,[2,3] seismic noise,[4–12] and ocean acoustics.[13–20] The approach of inferring the Green's function between two receivers from noise cross-correlations is referred to here as ocean acoustic interferometry (OAI), due to its relationship to classical and seismic interferometries, where interferometry refers to the determination of information from the interference phenomena between pairs of signals.[11] Several source types have previously been used for OAI: active, ocean wave, biological, and ship. The relationship between the cross-correlation of sound from a column of active sources in the ocean recorded by receivers in the same plane, and the Green's function between the receivers has been demonstrated theoretically and through simulation.[13,18] Sabra *et al.*[16] cross-correlated biological noise (croaker fish) from 150 to 700 Hz data. They obtained the direct arrival between hydrophones in a bottom array and used these arrival times for array self-localization. Using a vertical array of hydrophones, ocean surface wave noise cross-correlation was used to extract seafloor structure via passive fathometry.[17,19,20]

Roux *et al.*[14] showed experimentally that for a ship track passing through the end-fire region of a pair of hydrophones, the signal from the end-fire region dominates the cross-correlation. They extracted the direct arrival between the hydrophones. Simulations for sources (ships) at various ranges along the hydrophone end-fire direction showed that the cross-correlations emphasize different Green's function arrival paths, depending on the range.[14] The Green's function that is recovered is therefore not a true Green's function because each cross-correlation peak differs from that of the corresponding Green's function arrival peak by a path dependent amplitude factor; it is therefore termed an "amplitude shaded" Green's function.

Although the theory prescribes a uniform noise distribution, good approximations of the arrival structure of the actual Green's function can still be obtained from the cross-correlation time derivative, termed the *empirical Green's function* (EGF), even for nonuniform noise distributions.[4,21,22] To obtain an EGF For ship dominated noise without directional bias, the observation time must include several ship tracks passing through the end-fire region.[14] The ocean is nonstationary, suggesting that OAI over short time periods, such as a few minutes, is sufficient if instantaneous EGFs are desired. However, the need to average over multiple ship tracks requires longer observation times, and hence an "average" EGF over a long observation time (24 h) is obtained here. When using noise from breaking waves to extract EGFs a short observation time can be used. The theory here assumes that sources all have the same amplitude and frequency contents. Nearby ships tend to be louder, and larger ships have spectra that are dominated by lower frequencies. Time and frequency preprocessing are carried out to minimize these effects.

OAI of 20–100 Hz noise is considered in detail here. Data were collected on three L-shaped arrays from 31 Au-

[a]Also at the School of Mechanical Engineering, The University of Adelaide, Australia. Present address: Institute of Geophysics, Victoria University of Wellington, New Zealand. Electronic mail: laura.brooks@vuw.ac.nz

gust to 3 September 2006 during the Shallow Water 2006 (SW06) experiment. Tropical Storm Ernesto[23] passed through the area on September 2, creating a richer noise field that is well suited for extracting EGFs.

At frequencies below about 100 Hz the noise field is usually dominated by shipping noise.[24] Nearby shipping favors higher grazing angles, while distant shipping favors more horizontally traveling wavefronts. During Tropical Storm Ernesto local ships left the region. Thus, the shipping portion of the noise field was dominated by distant vessels. For a horizontal set of hydrophones, the direct path EGF will be dominated by noise from distant ships.

The passing of Ernesto resulted in more acoustic energy at low frequencies from breaking waves and this noise is also distributed at higher propagation angles, as is evident from the beamforming on the vertical array. The higher propagating angles of the breaking wave noise enable the extraction of EGFs for more vertically traveling paths. Because of the higher noise levels and richer angular distribution from breaking wave noise and the more azimuthally uniform time-averaged shipping noise field, the EGFs extracted during the storm match the actual Green's functions more closely.

Thus, through careful processing and a longer averaging time, combined with a more evenly distributed noise field, it is possible to extract not only the direct arrivals but also higher order multiples in the water column. Furthermore, these arrivals tend to extend farther in range than previous results, with sharp arrivals and good signal-to-noise ratios.

II. THEORETICAL BACKGROUND

Both shipping noise and ocean wave generated noise originate at or near the ocean surface, and hence it is assumed that the 20–100 Hz noise considered here can be modeled as a set of sources that are uniformly and densely distributed within a horizontal plane near the surface of a waveguide. The cross-correlation of the signals recorded at two receivers, A and B, can therefore be derived following the stationary-phase methodologies of Refs. 18 and 25:

$$C_{AB}(\omega) = |\rho S(\omega)|^2 n \int \int G(\mathbf{r}_A, \mathbf{r}_S) G^*(\mathbf{r}_B, \mathbf{r}_S) dx dy, \qquad (1)$$

where $S(\omega)$ is the ship or wave source spectrum, ρ is the density of the medium, n is the number of sources per unit area, $G(\mathbf{r}_\psi, \mathbf{r}_S)$ is the Green's function between the source, S, and receiver, ψ, $*$ denotes the complex conjugate, and x and y are the horizontal axes parallel and perpendicular, respectively, to the vertical plane containing A and B.

Application of the method of stationary phase to Eq. (1),[15,18,25,26] as well as summation over all stationary points, yields

$$C_{AB}(\omega) = in|S(\omega)|^2 \sum_{\chi_s} \left(\frac{\Gamma^{b_A + b_B} c \rho}{2\omega \cos\theta} G_f(R(\chi_s)) \right), \qquad (2)$$

where χ_s are the stationary points, c is the wave velocity, f is the acoustic frequency, $\omega = 2\pi f$ is the angular frequency, Γ is the bottom reflection coefficient, b_ψ is the number of bottom bounces for a given path, θ is the acute angle between the ray path and the vertical, $G_f(R) = e^{ikR}/4\pi R$ is the three-dimensional Green's function within a homogeneous medium, where k is the wave number and R is the distance from the source, and $R(\chi_s)$ is the path length difference between a wave traveling from χ_s to A, and a wave traveling from χ_s to B. Note that the stationary points, χ_s, satisfy the relationship $\theta_A = \pm\theta_B$. The positive relationship between θ_A and θ_B only occurs when the path to the furthest receiver passes through the closer receiver, hence the relationship between the summed cross-correlations and the Green's function between the receivers. The negative relationship corresponds to stationary-phase contributions from cross-correlations between a wave that initially undergoes a surface reflection, and one that does not.[15,18] Since ship and wave sources are near the ocean surface, these spurious arrivals will converge to almost the same time delay as the true Green's function paths, and due to the long wavelengths, will not be observed as separate peaks. The model assumes that all sources have the same spectrum. The ocean wave ambient noise field is reasonably uniform, but the ship noise field is more discrete and each ship has a different spectrum. This will cause an unknown bias in the summed cross-correlation; however, averaged over a long observation time, this bias is reduced as each ship covers a large azimuthal area. The theory presented here has also neglected curvature of ray paths due to refraction, but it has been shown by others[25] that the stationary-phase argument generalizes to a heterogenous medium with smooth velocity variations.

The cross-correlation in Eq. (2) can therefore be seen to produce an amplitude and phase shaded Green's function. The amplitude shading is dependent on the travel path through the $\Gamma^{b_A+b_B}$ and $\cos\theta$ terms, and also contains constant and frequency dependent components. The $1/\omega$ factor phase shading in Eq. (2) means that the time domain Green's function is approximately proportional to the derivative of the summed cross-correlations:[5,15,18,21]

$$\frac{\partial C_{AB}(t)}{\partial t} \sim -[G_{AB}(t) - G_{AB}(-t)]. \qquad (3)$$

The raw cross-correlation, rather than its time derivative, is often used as an approximation to the Green's function[14,17,19,27] because this is better in certain environments.[25,28]

III. EXPERIMENT

The SW06 experiments were conducted off the New Jersey shelf. The data considered here, from measurements of opportunity, were collected from August 31 to September 3 on three L-shaped arrays: SWAMI52, SWAMI32, and Shark. L-shaped arrays were used as these allow for approximation of travel paths between bottom mounted hydrophones, as well as approximation of higher grazing angle paths between bottom hydrophones and those located within the watercolumn. Array locations and orientations are shown in Fig. 1(a), and configurations are detailed in Table I. The orientations of the horizontal portion of each array varied, and thus each array was sensitive to a different propagating environment. The SE-NW and S-N oriented SWAMI52 and Shark arrays

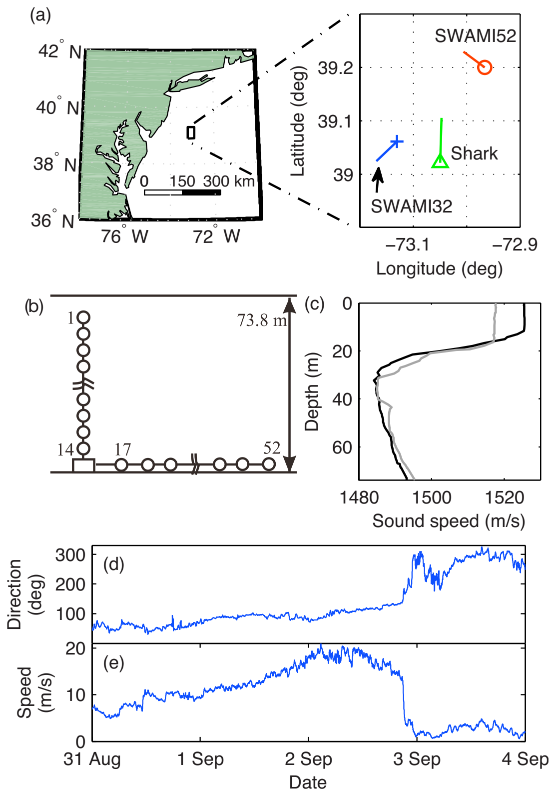

FIG. 1. (Color online) (a) Geographic location of experimental site (black rectangle) on New Jersey Shelf, with magnified view showing the relative locations of SWAMI52, SWAMI32, and Shark. The lines departing each VLA show the HLA orientation. The array length is scaled by a factor of 20. (b) SWAMI52 geometry and hydrophone numbering system. (c) Sound speed profiles near SWAMI52 for August 30 (black) and September 6 (gray). (d) Wind direction and (e) wind speed, from R/V *Knorr* ship records, from August 31 to end of September 3.

were sensitive to upslope propagation of noise from deeper waters, while the SWAMI32 array was oriented along the shelf (NE-SW).

The horizontal line arrays (HLAs) were all located on the seafloor. All vertical line array (VLA) hydrophones and the Shark HLA hydrophones are evenly spaced. SWAMI52 interhydrophone distances increase from the center, and SWAMI32 HLA interhydrophone distances increase from the hydrophone 13 (H-13) end, respectively. A sketch of the SWAMI52 geometry is shown in Fig. 1(b). Sound speed profiles that were recorded near SWAMI52 on August 30 and September 6 are shown in Fig. 1(c). Example schematics of the raypaths that will be approximated from the cross-correlations are shown in Fig. 2.

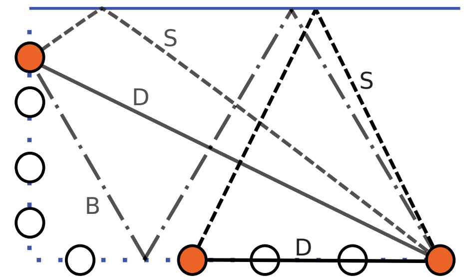

FIG. 2. (Color online) Direct (D, solid), surface-reflection (S, dashed), and surface-bottom-reflection (B, dashed-dotted) raypaths from HLA hydrophone (far right) to second HLA hydrophone (black paths, B does not exist), and to VLA hydrophone (gray paths).

Tropical Storm Ernesto passed through the experimental area during the data collection period, leading to large sea states and high winds. The wind direction and speed from August 31 to September 3 are shown in Figs. 1(d) and 1(e). Predominantly easterly winds gradually built up over August 31 and September 1 to a 20 m/s peak early on September 2, and then remained high until late in the day, when they dropped rapidly once the storm had passed. The decrease in speed was accompanied by a change in wind direction to south and west.

IV. ANALYSIS OF DATA PREPROCESSING METHODS

Time and frequency domain preprocessing methods were applied to the raw data to emphasize broadband ocean noise. The preprocessing techniques considered here were analyzed using the data collected on SWAMI52 throughout September 2 (Zulu time). No towed source experiments were undertaken on this day, because of Ernesto, and therefore ocean noise over a large frequency bandwidth could be considered. The data were stored and analyzed in 140 portions, each 10 min and 14 s (10:14 min) duration.

Short (10:14 min) cross-correlations were unstable above the thermocline, likely due to sound speed fluctuations resulting from the elevated levels of swell and mixing associated with Ernesto. If the noise field had been isotropic and sufficiently strong, OAI could have been performed over periods that were sufficiently short for the environment to be

TABLE I. Details of array configurations.

			VLA		HLA	
	Water depth (m)	No. hydrophones	Length (m)	Hydrophones[a]	Length (m)	Hydrophones[b]
SWAMI52	73.8	52	56.81	1:14	230	17:52
SWAMI32	68.5	32	53.55	1:10	256	13:32
Shark	79	48	64.25	0:12	465	16:47[c]

[a]Lowest numbered hydrophone is uppermost in the array. Extra hydrophones tied off just above the frame (SWAMI52: H-15 and H-16, SWAMI32: H-11 and H-12, and Shark: H-13–H-15).
[b]Lowest numbered hydrophone is closest to the array except for Shark, which is opposite.
[c]Data from H-15 and H-46 were discarded due to inconsistencies with other data.

considered stationary. The temporal change in cross-correlation could then have been related to environmental changes, in particular, changes in temperature in the upper waveguide, and tidal changes. However, discrete ships are a significant noise source here, and therefore the cross-correlations had to be performed over a long time period so that specific ship sources did not dominate (see Sec. VI).

Comparisons of time and frequency domain normalization techniques by Bensen *et al.*[12] concerned seismic noise, which is often dominated by high amplitude earthquakes and lower frequencies. Since other physical processes dominate ocean noise, the effect of these normalization techniques on the resulting EGFs will also differ. A comparative study of several techniques to the current data set was undertaken for both frequency (Sec. IV C) and time (Sec. IV D) domain preprocessing. Frequency normalization using a smoothed amplitude spectrum, and one-bit time normalization were then chosen as the preferred preprocessing methods.

A. Removal of main contamination

Depending on the particular time interval, some of the September 2 data exhibited high amplitude midfrequency signal from fixed location sound sources, amplitude clipping, and low frequency energy bursts. Electrical noise could manifest as high amplitude tonals at the hydrophone operation frequency and its harmonics, and/or as Gaussian noise across a wider frequency band. Impact noise from a fish colliding with a hydrophone or something else tapping the hydrophone array would likely be observed as sharp amplitude peaks in the time domain, and energy would be smeared across the frequency spectrum at this time. Signals from any ships near the array throughout the day would be recorded as discrete high amplitude tonals.

All discrete signals have a difference in direct path length to each hydrophone, which is less than or equal to the direct path between the hydrophones, and may be visible in the cross-correlation as spurious precursory arrivals. Preprocessing, which includes choice of bandwidth as well as time and frequency domain normalizations, ameliorates these effects (see Secs. IV B–IV D).

B. Spectra and coherence

Only signals that are received by both hydrophones will sum coherently to give a peak in the cross-correlation function. Both the signal amplitude and coherence are therefore considered here. Since the underlying statistics of the data are nonstationary, spectra and coherence over short periods are examined. Spectrograms of the signals received by H-52, and coherograms (coherence plotted as a function of frequency and time) of the signals recorded on H-52 and H-40, which are separated by 97.74 m, are shown in Fig. 3. The mean spectra and coherence for 1:33 min intervals were calculated using 2 s Hanning windowed data segments and 50% overlap. The mean of each set of spectra and coherences is shown on the far right.

High amplitude signals with high coherence are apparent at regular time intervals in the 200–410 Hz frequency range, as shown in Figs. 3(a) and 3(c). These signals are from three

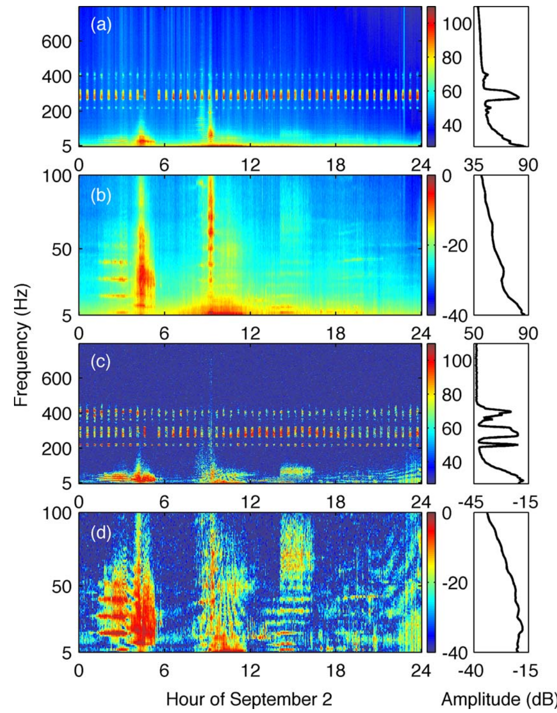

FIG. 3. (Color online) Spectrograms (dB) of signals recorded on H-52, using the entire September 2 data: (a) 5–800 and (b) 5–100 Hz. Coherograms (dB relative to unity linear coherence) of the data recorded on H-52 and H-40: (c) 5–800 and (d) 5–100 Hz. The average of each set of spectra or coherences is plotted to the right of each figure.

fixed location sound sources. Low signal amplitudes and coherence are observed at frequencies above 420 Hz, and also from 100 to 200 Hz. Below 100 Hz both the amplitude and coherence of the received signals are higher. This is expected since the attenuation of lower frequency ocean noise is less over long distances. A banded structure consisting of high amplitude tonals is observable in both the low frequency spectrogram and coherogram, Figs. 3(b) and 3(d), at a range of frequencies at different times throughout the day (e.g., 1:30–3:30Z and 13:30–15:30Z). This banded structure is indicative of ship noise at low frequencies.

Since the signals, apart from those emanating from the fixed sound sources, exhibit negligible amplitude and coherence above 100 Hz, the data were bandpass filtered to 20–100 Hz. The lower limit of 20 Hz was selected because frequencies below this have insufficient resolution for more closely spaced hydrophone pairs that are separated by only a few meters.

Beamformed data of 10:14 min duration, recorded on the SWAMI52 VLA at the start of each day of August 31–September 3, are shown in Fig. 4. The critical angle at the bottom can be observed from the beamformer output to be about 25°, corresponding to a sediment sound speed of 1650 m/s. The extraction of the critical angle from the beamformer seems more straightforward than extracting it from the noise cross-correlation.[29] The data from the two mornings before the storm, (a) and (b), show more horizontally traveling wave fronts, as would be expected for a noise field dominated by distant shipping and distant breaking waves. The data from the morning of the storm and the morning after, (c) and (d), show a significant increase in

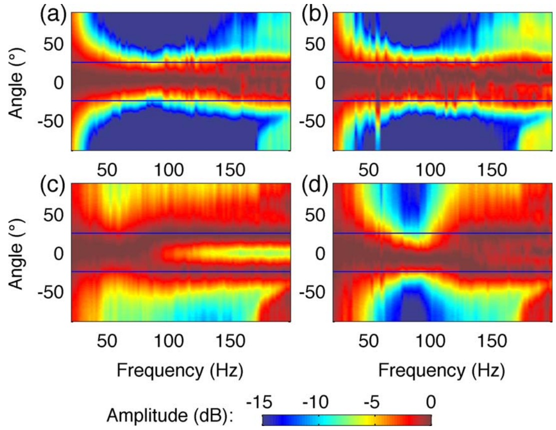

FIG. 4. (Color online) Beamformer output, normalized to maximum at each frequency, from 10:14 min of SWAMI52 VLA data at the start of (a) August 31, (b) September 1, (c) September 2, and (d) September 3. The horizontal lines are overlayed at $\pm 25°$.

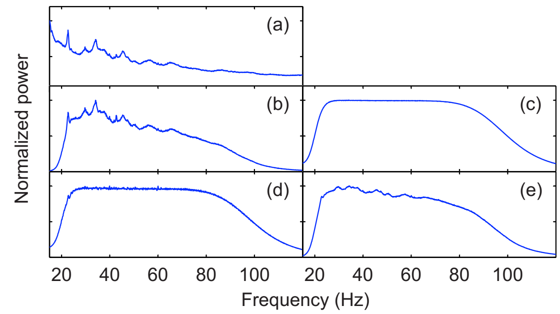

FIG. 5. (Color online) Normalized (linear) spectra of the September 2 signals recorded on H-40 (a) before prefiltering and [(b)–(e)] after prefiltering. Prefiltering methods are (b) bandpass and time domain filters only, (c) absolute whitening, (d) smoothed whitening, and (e) partial whitening (β=1).

higher frequency energy at and above 25°, suggesting that there is a significant increase in locally generated wave noise during the storm.

C. Frequency domain normalization

Frequency domain normalization has the dual purpose of broadening the signal bandwidth by placing higher emphasis on low amplitude signals, and of decreasing the negative impact of discrete sources. For the purpose of comparing frequency domain normalization methods, the effects of high amplitude temporal peaks, such as those observed around 4:30Z and 9Z in the low frequency spectrogram and coherogram, were minimized by setting all values of amplitude greater than 50% of the signal standard deviation to this value,[7,30] a process described as "threshold clipping," and explained further in Sec. IV D.

1. Normalization methods

OAI was performed using five different frequency domain preprocessing methods:

(a) no frequency domain preprocessing;
(b) bandpass filter, no frequency domain amplitude normalization;
(c) bandpass filter and whiten by normalizing over the entire frequency range (20–100 Hz), known as absolute whitening;
(d) bandpass filter and normalize by a smoothed version of the amplitude spectrum, known as smoothed whitening; and
(e) bandpass filter and partially normalize the data by the sum of the signal magnitude at that frequency and a mean amplitude dependent constant:

$$S(\omega) = \frac{S(\omega)}{|S(\omega)| + \beta\overline{|S|}}, \tag{4}$$

where $\overline{|S|}$ is the mean amplitude over the entire frequency range, and β determines the degree to which the data are whitened [β=0 is equivalent to absolute whitening (c), and $\beta=\infty$ to no normalization (b)].

The effect of applying each normalization technique to H-40 data can be seen in Fig. 5. Bandpass filtering without frequency normalization, method (b), maintains the general characteristics of the amplitude peaks and decay with frequency seen in the raw data, method (a). Absolute and smoothed whitening, methods (c) and (d), respectively, give approximately equal energy across the frequency band. Partial whitening, method (e), reduces extraneous tonals, but also places emphasis on signals of higher coherence (lower frequency).

2. Application to data

Data were preprocessed using each of the methods outlined in Sec. IV C 1. Individual cross-correlations were calculated and normalized by their peak value before summing so that the overall cross-correlation is not dominated by high amplitude cross-correlations from only part of the day. The cross-correlations between H-52 (tail-end HLA hydrophone) and all other hydrophones, summed over September 2, using smoothed-whitening filtering, method (d), are shown in Fig. 6(a).

The HLA cross-correlations are plotted as a function of distance from H-52. The VLA cross-correlations, which are offset by the horizontal distance between H-52 and the VLA hydrophones, are plotted as a function of height from the seafloor (note that the two vertical axes have different scales). The direct (D), surface-reflected (S), and surface-bottom-reflected (B, VLA cross-correlations only) travel times between each hydrophone, which are shown as dotted lines, were determined using OASES.[31]

Peaks in the cross-correlation are evident at both the direct and surface-reflected travel times. The EGF envelope in Fig. 6(b), on a logarithmic scale, reveals the surface-bottom reflected path to the lower VLA hydrophones.

The EGF envelope for the case of bandpass filtering only, method (b), shown in Fig. 6(c), shows only minor differences to that for smoothed whitening. Due to the higher proportion of low frequency energy, the arrivals are less sharp and the background noise level is slightly higher. In addition, the surface-reflected path is not as clear at the closer hydrophones (40–120 m). The raw signals have greater amplitude at lower frequency and this naturally assists the EGF when no frequency domain normalization is applied; the lower coherence signals have lower amplitude

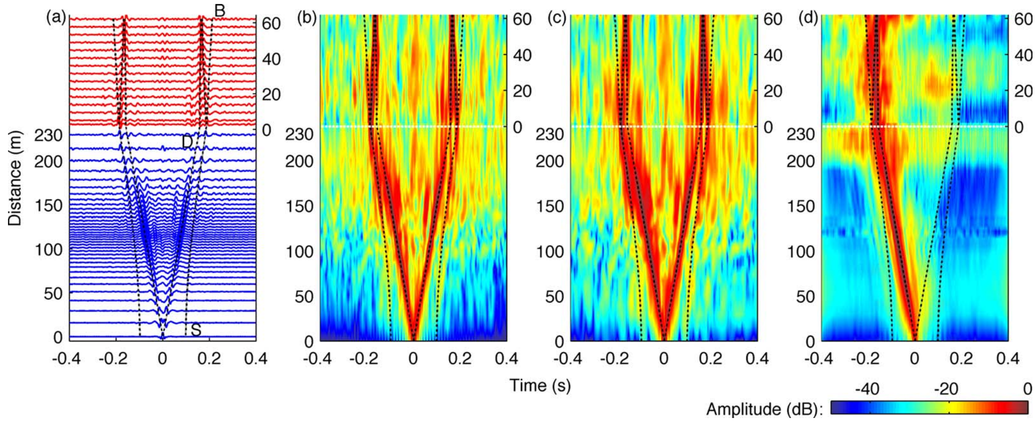

FIG. 6. (Color online) (a) Cross correlations between H-52 and all other hydrophones for September 2 data using smoothed-whitening frequency filtering (20–100 Hz bandwidth). [(b)–(d)] EGF envelope (dB relative to maximum value): (b) with smoothed whitening (20–100 Hz bandwidth), (c) with no frequency normalization (20–100 Hz bandwidth), and (d) with no frequency domain filtering or normalization. The lower traces are from EGFs with HLA hydrophones; their distances from the tail hydrophone (H-52) are shown on the left side axis. The upper traces are EGFs with VLA hydrophones; their vertical distance from the seafloor is shown on the right side axis, which is offset by the horizontal distance of the VLA from the HLA tail. The simulated travel times between the hydrophones were calculated using OASES and are overlaid as dotted lines.

and will therefore have less overall influence on the cross-correlated signal. This explains why a reasonable EGF can be determined when no spectral normalization is performed. The EGF envelope for no frequency domain filtering, method (a), shown in Fig. 6(d), gives a poor representation of the Green's function. A low frequency signal below 20 Hz from the southeast dominates the EGF to such an extent that only the direct acausal path is obtained. The EGF envelopes for absolute and partial whitening, methods (c) and (e), are not shown, but their characteristics lie between that of Figs. 6(b) and 6(c).

Smoothed whitening was selected as the optimal frequency domain filtering method for the data collected. Bensen *et al.*[12] compared no normalization and smoothed whitening for cross-correlations of seismic data and found that the improvements gained by normalization were substantially greater than here. Appropriate selection of the data bandwidth affected the result more than any frequency domain normalization because above the 100 Hz low-pass frequency the cross-correlation has almost no coherence, and therefore inclusion of higher frequencies adds to the noise floor. If no frequency domain filtering or normalization is applied this added noise is minimal, since the amplitude is negligible at higher frequencies. However, if the data are whitened but not bandpass filtered, signals of low coherence will be emphasized, and the resulting cross-correlation sum will be dominated by noise that requires very long averaging times to remove.

D. Time domain normalization

Various methods of time domain normalization have been used by others. One-bit time reversal normalization, where the sign (phase) of the waveform is retained but the amplitude is discarded, yields a higher signal-to-noise ratio than classical time reversal in some multiple scattering media.[32,33] A similar argument holds for cross-correlation analysis and therefore one-bit normalization is frequently used.[16,32,33] Another method of time domain normalization is to clip all signals above a certain threshold.[7] This minimizes the effect of energy bursts, but also retains more information than one-bit normalization. Gerstoft *et al.*[30] set their threshold as the minimum of the standard deviations measured over each day. For their data set this gave identical results to one-bit normalization. Bensen *et al.*[12] and Yang *et al.*[34] used temporally variable weighting functions. They claimed that these retain more small amplitude information and also allow for flexibility in defining the amplitude normalization in particular frequency bands.

1. Normalization methods

Six different time domain preprocessing methods and their applicability to 20–100 Hz ocean noise are compared here:

(a) no normalization;
(b) cross-correlate over short intervals with some degree of overlap, normalize the cross-correlations and then sum;
(c) clip the signal to a threshold;
(d) one-bit normalization;
(e) use of a rectangular central temporally variable weighting (RCTVW) function; and
(f) use of an exponential central temporally variable weighting (ECTVW) function.

Performing no normalization in the time domain sets a clear benchmark for the five other techniques. Cross-correlating over short intervals and then summing the normalized cross-correlations is more effective for shorter intervals. Since the greatest distance between any two hydrophones is 230 m, the direct path should be observable in under 0.2 s; hence, to ensure sufficient time for reverberant paths to be captured, 0.4 s data segments were used, with 33% overlap.

A threshold of σ, one standard deviation, was chosen as the level to which the signal would be clipped for normalization technique (c). It was noted that the results were not

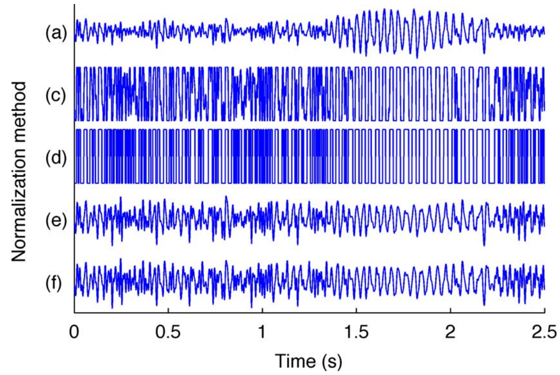

FIG. 7. (Color online) Preprocessed waveforms for 2.5 s of 20–100 Hz bandpass filtered data from H-40 (at 12:48:45Z) with normalization method: (a) none, (c) threshold clipping, (d) 1 bit, (e) RCTVW, and (f) ECTVW.

highly sensitive to the chosen threshold. Mathematical descriptions of one-bit normalization, RCTVW, and ECTVW are included in the Appendix.

2. Application to data

Example waveforms resulting from application of each time-normalization method to 2.5 s of H-40 data are shown in Fig. 7. Higher energies are observed in the time period 1.4–2.1 s, as can be seen in Fig. 7(a), and these amplitudes are all successfully reduced by the time-filtering methods, as shown in Figs. 7(c)–7(e). Normalization technique (b) is not shown here as this normalization is only applied after cross-correlating the data.

EGF envelopes for September 2 for each time-normalization method are shown in Figs. 8(a) and 8(b). The same line style has been used in the figure for all results because they are too similar to be individually discerned. The horizontal distance between (a) the HLA hydrophones H-52 and H-48 is 31.31 m, and the horizontal distance between (b) the HLA hydrophones H-52 and H-8 (located in the VLA) is 230 m. For the two closely spaced hydrophones shown in Fig. 8(a), large EGF peaks exist at the direct ray travel time, and smaller peaks at the surface-reflected travel time. The background noise is consistently low, except for one high peak at a time just less than the positive direct arrival. This could be due to a nonuniform source distribution. For the two further spaced hydrophones shown in Fig. 8(b), the EGF envelope once again peaks at the direct and surface-reflection travel times. A smaller peak can also be seen at the acausal surface-bottom travel time (i.e., the bottom-surface-reflected path from H-8 to H-52). The signal-to-noise ratio is poorer than for the more closely spaced hydrophones, but this is to be expected since decay and spreading of signals increase with distance.

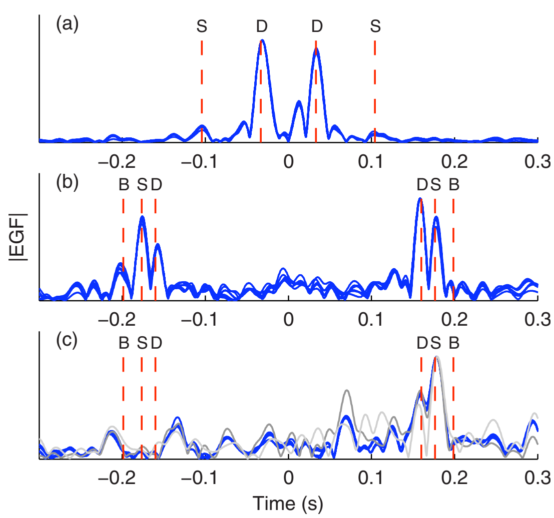

FIG. 8. (Color online) EGF envelopes, |EGF|, for all time-normalization methods for H-52 and (a) H-48 (entire day with 51.32 m horizontal separation), (b) H-8 (entire day with 230 m horizontal separation), and (c) H-8 (10:24 min from 8:30Z). Simulated travel times of direct (D), surface (S), and surface-bottom (B) paths are shown as vertical dashed lines. In (c) results for no normalization and short interval EGFs are shown in dark and light gray, respectively.

The results from Figs. 8(a) and 8(b) suggest that time normalization has little influence on EGFs for this data set. Time normalization is important for seismic cross-correlations[8,12] since otherwise the results can be dominated by earthquakes. Although the ocean noise field is not perfectly diffuse, there are no equivalently energetic events for the frequency band considered, and nearby shipping is minimal on September 2. This and the intrinsic averaging introduced by summing over the entire day are two reasons why time domain normalization shows negligible benefit here.

If OAI were carried out over a time period insufficient to average out energetic events, the benefits of normalization would be greater. Consider the 10:14 min EGFs between H-52 and H-8 in Fig. 8(c). The EGFs peak at the positive direct and surface-reflected travel times only, indicating that the dominant sound field is from the tail end of the array (the northwest direction). Distinct peaks seen at −0.22, −0.14, and 0.07 s are the result of discrete sources. Since high amplitude events, which are reduced in the normalization process, are not averaged out in the shorter cross-correlation time period, the EGF envelope without normalization, method (a), and EGFs from cross-correlating over short periods and summing the normalized results, method (b), both have a higher noise level than the results for data that are normalized before cross-correlation.

Since time domain normalization techniques (c)–(f) all give similar results, and one-bit normalization is the least computationally intensive, it was selected for further processing and analysis of the data.

The EGFs between H-52 and all other hydrophones for 20–100 Hz bandpassed, one-bit normalized, smoothed whitened September 2 data are shown in Fig. 9(a). The Green's function, which was simulated using OASES, is shown convolved with a 20–100 Hz box car pulse in Fig. 9(b) for comparison purposes. The assumed model sediment density, $\rho = 1.69\ \mathrm{g/cm^3}$, was approximated from grab samples in the array vicinity,[35] and a sediment sound speed of $c = 1650\ \mathrm{m/s}$, estimated from the critical angle suggested by the VLA beamformer, was also assumed. Note that exact bottom properties are not critical as the simulations are only used here to calculate travel times, not amplitudes, of ocean-only paths. The direct arrival peaks are positive and the reflected arrival peaks are negative, which is due to the phase

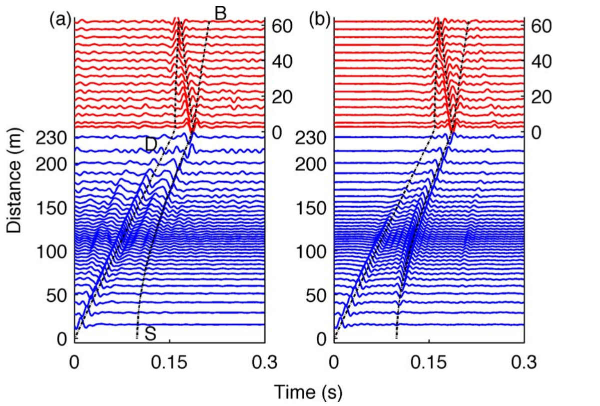

FIG. 9. (Color online) (a) EGFs between H-52 and all other hydrophones for September 2, with simulated travel times of direct (D), surface (S), and surface-bottom (B) paths shown as dotted lines. (b) Simulated Green's functions convolved with a 20–100 Hz bandwidth linear source. Vertical axis format is the same as in Fig. 6.

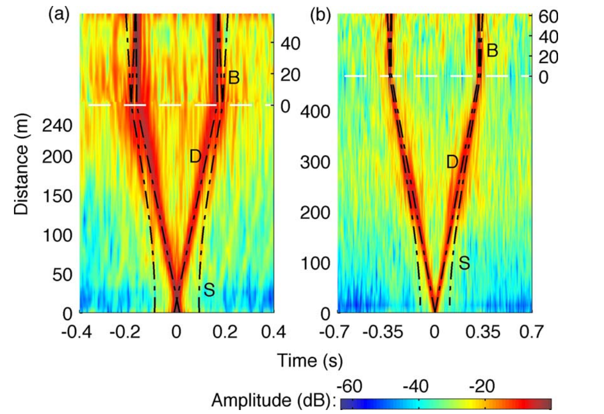

FIG. 11. (Color online) September 2 EGF envelopes (dB relative to maximum amplitude) for (a) SWAMI32, with respect to H-30, and (b) Shark, with respect to H-16. Vertical axis format is the same as in Fig. 6.

change at the surface. The amplitudes are not exact, though this is expected since the source field is not diffuse. The surface-reflected arrivals are apparent in the EGFs for distances greater than about 50 m. They are not observable at closer ranges, where they would be more steep, because the vertically propagating noise is weaker.

If a cross-correlation is started or finished part way through a ship's track, the EGF may be biased. Tapering of the cross-correlation amplitudes toward the start and end of the cross-correlation was therefore considered; however, for the given data set and long cross-correlation times, tapering was seen to have negligible effect.

V. GEOMETRIC COMPARISONS

Examples of EGF envelopes with respect to hydrophones other than the outermost HLA hydrophone, H-52, are shown in Fig. 10. Due to the steeper grazing angle to the furthest hydrophone, EGFs with H-34, a central HLA hydrophone, shown in Fig. 10(a), do not yield as much information about the surface-reflected path as do EGFs with H-52, shown in Fig. 9(d). Figure 10(b) reveals that EGFs with VLA H-10 show the surface-reflected path, at slightly larger times than the dominant direct path, for distances of 0–150 m

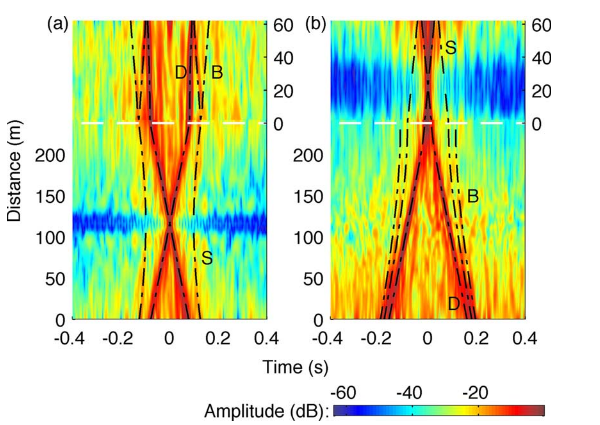

FIG. 10. (Color online) September 2 EGF envelope (dB relative to maximum amplitude) for SWAMI52 with respect to (a) H-34 and (b) H-10. Vertical axes are the same as in Fig. 6.

from the tail end of the HLA; however, the surface path is not as clear as that obtained when cross-correlating with H-52, which is likely due to either the decreased stability in the environment at the shallower depth of H-10, or the increased motion of the VLA hydrophones relative to the HLA hydrophones. The bottom-surface-reflected arrival from H-10 to the HLA hydrophones is also observable at a time just after the surface-reflected path, but the acausal path from the HLA to H-10 is not observable.

The September 2 EGF envelopes for SWAMI32 and Shark are shown in Fig. 11. The SWAMI32 EGFs are with respect to H-30 rather than the tail hydrophone due to high noise on the outer two hydrophones. The high noise levels are attributed to channel switching.[36] Like the SWAMI52 results shown in Fig. 9(d), the SWAMI32 and Shark array EGFs show both the direct and surface-reflected paths. The results in Figs. 9–11 show that, for all arrays, although the direct path dominates for more closely spaced hydrophones, the relative amplitude of the surface-reflected path increases at greater distances. These relative amplitudes depend on array geometry, modal distribution of acoustic energy, roughness at the surface, and, importantly, the impedance at the seafloor. As such, a relationship between the relative amplitudes of the paths and the critical angle could potentially be determined.[29]

Unlike the tapered spacing of the SWAMI52 and SWAMI32 HLA hydrophones, the Shark HLA hydrophones are evenly spaced at 15 m intervals. The September 2 EGFs between all HLA pairs separated by 345 m are plotted in Fig. 12(a). The traces are similar, and all display EGF peaks at approximately ±0.24 s. The median value of the signals is plotted against a shaded area encompassing the range of all signal values in Fig. 12(b). A magnified view of part of the signal is provided in Fig. 12(c) and shows that the signal variation is minimum near the direct path travel time.

VI. TEMPORAL VARIATIONS

The September 2 data EGFs with H-52 were compared with those from adjacent days, and are shown in Fig. 13. The September 2 data, shown in Fig. 13(c), peak at the expected direct and surface-reflected paths and exhibit the least back-

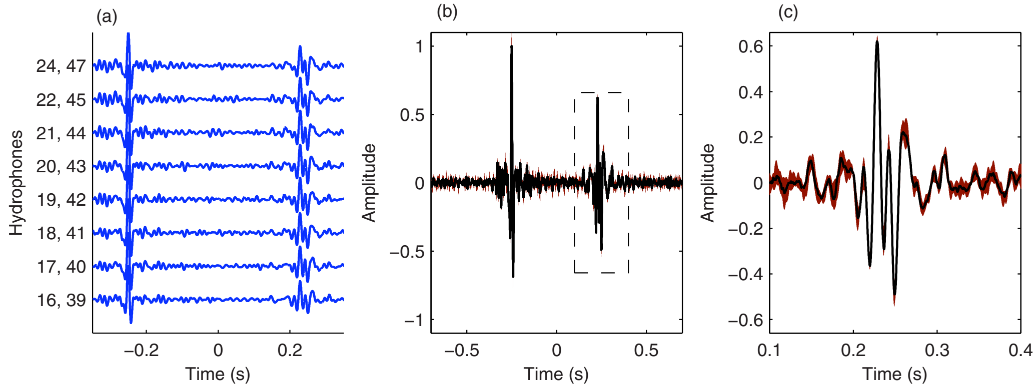

FIG. 12. (Color online) (a) September 2 EGFs for Shark hydrophone pairs separated by 345 m. (b) The median EGF from (a) overlies a shaded region between which all values lie. (c) Data from the dashed box in (b) are magnified.

ground noise. Results from September 1, shown in Fig. 13(b), are not as clear as those from September 2, but are still better than from September 3 and August 31, shown in Figs. 13(d) and 13(a), respectively, suggesting that the sound field is more diffuse during the storm.

Short time EGFs were calculated for data from pairs of hydrophones for all three arrays from 0Z August 31 to 12Z September 3. SWAMI52 hydrophones H-52 and H-17, SWAMI32 hydrophones H-30 and H-15, and Shark hydrophones H-16 and H-35 were chosen as their separation distances are all similar (between 200 and 285 m). Time segments corresponding to one data file were used for SWAMI52 and SWAMI32 (10:14 and 6:24 min, respectively), and quarter files (8:34 min) were used for Shark. The corresponding EGF envelopes are plotted as a function of time in Figs. 14(a)–14(c), along with the EGF envelope of the summed normalized cross-correlations over the 84 h period.

The EGF envelope is dominated by discrete sources, as indicated in Figs. 14(a)–14(c) by the high amplitude peaks that occur throughout the days at times less than the direct interhydrophone travel times. Hydrophone spectrograms from times corresponding to the largest peaks are dominated by a banded structure indicative of ship noise. As an example, spectrograms of 60 s duration from 3:36:40Z August 31 for SWAMI52 H-52 and SWAMI32 H-30 are shown in Figs. 14(d) and 14(e). Noise from a large ship, with a primary tonal at just under 40 Hz, dominates both spectrograms. The ship is visible as a peak in the EGF envelope for all three arrays from 0 to 4Z August 31. It was ascertained from the time of the EGF envelope peak that during this period the ship moved from southwest of the arrays to north of the arrays. The peak in EGF time due to a ship changes with the ship's azimuth to the array, with peak times approaching the interhydrophone travel time as the ship approaches end-fire. Hence, the signals from a ship are apparent as curves when plotted as a function of experimental and correlation times. The "pattern" of curves that is visible in Figs. 14(a)–14(c) is therefore due to a multitude of ship tracks. Most shipping occurred along the coast and this is apparent from the greater proportion of ship tracks visible at positive travel times in Figs. 14(a) and 14(b), corresponding to NW and SW directions for SWAMI32 and SWAMI52, respectively. The Shark array was parallel to the coast, and as such, the ship tracks in Fig. 14(c) do not appear to have a preferred direction.

Toward the end of September 1 and on September 2 the EGF envelope is more stable, as observed by the main peaks in the EGF being more consistently closer to the dashed interhydrophone travel times and also by the amplitude and number of smaller peaks in the EGF being reduced. Fewer shipping tracks are seen, and faint arrivals are observable at the interhydrophone travel times. This is during the period of high wind [see Fig. 1(e)] and sea conditions from Tropical Storm Ernesto. The reduction in number of nearby ships and the increase in wave energy result in a greater proportion of

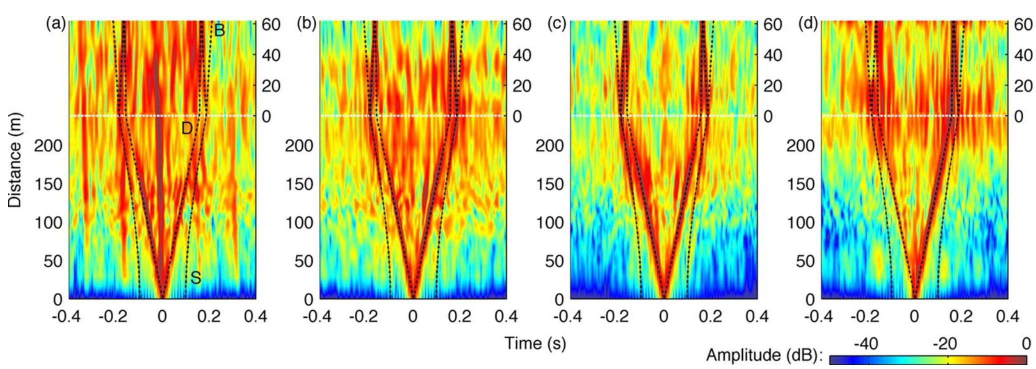

FIG. 13. (Color online) EGF envelope (dB relative to maximum amplitude) with respect to H-52 for (a) August 31, (b) September 1, (c) September 2, and (d) the first 12 h of September 3. Vertical axes are the same as in Fig. 6.

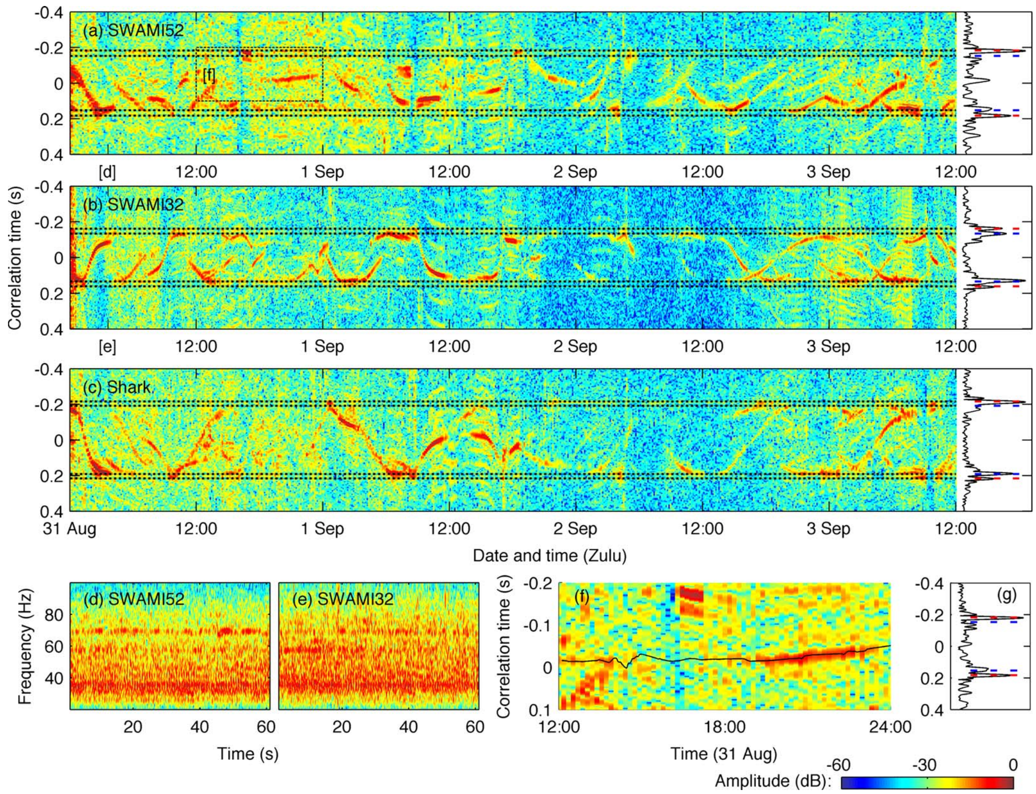

FIG. 14. (Color online) EGF envelope (dB relative to maximum amplitude) plotted for (a) SWAMI52 H-52 and H-17 (230 m separation), (b) SWAMI32 H-30 and H-15 (200 m separation), and (c) Shark H-16 and H-35 (285 m separation). Simulated direct and surface-reflected travel times (dashed lines) faintly overlayed. The envelope of the time derivative of the sum of all cross-correlations (normalized by their peak amplitudes to minimize the effects of dominant signals) is shown at the right of each plot. [(d)–(e)] 20–100 Hz spectrograms from 3:36:40Z August 31 for SWAMI52 H-52 and SWAMI32 H-30 [times denoted on (a) and (b) time axes as "d" and "e"], respectively. (f) Enlarged view of SWAMI52 EGF envelope [boxed area from (a)] showing a dominant near-side signal, with calculated travel time difference (black line) from R/V *Oceanus* to the hydrophone pair. (g) The envelope of the time derivative of the sum of all cross-correlations, excluding the period 12–24Z August 31 for SWAMI52 data.

acoustic energy in the ocean at these lower frequencies being from breaking waves and cumulative noise from distant shipping, and therefore the noise field is more diffuse. During this period faint peaks are frequently observed at times corresponding to the simulated surface-reflection travel times, such as between 22Z September 1 and 3Z September 2 in the acausal signal of Fig. 14(c).

Although the short term EGF envelope rarely yields the modeled interhydrophone travel time, based on the measured sound speed profile, throughout the 84 h period, the EGF envelopes of the summed cross-correlations for this period do peak at times near the simulated travel times, as shown at the far right of Figs. 14(a)–14(c). The surface-reflected path is particularly strong. This is because the EGF is dominated by nearby ships, and these shorter ranges favor higher acoustic grazing angles.

A strong signal is observed at a correlation time of slightly less than zero for all EGFs for August 31 in Fig. 13(a), suggesting that there is a high amplitude signal from near broadside (either SW or NE) of the array during that day. A corresponding peak in the summed SWAMI52 EGF envelope is seen at −0.0175 s at the far right of Fig. 14(a). The EGFs reveal that this peak is a result of signals from 12–14Z and 18–24Z on August 31 [see box "f" and Fig. 14(f)]. The Shark and SWAMI32 EGF envelopes do not show a strong signal at these times. Hence the dominant signal seen in the SWAMI52 data is likely from a source significantly closer to that array than the others. R/V *Oceanus* was located NE of SWAMI52 (in the region 39.25–39.28°N, 72.8–72.9°W) from 12 to 24Z August 31, about 10 km away. This is the closest that R/V *Oceanus* came to any of the arrays during the experiment. R/V *Oceanus* moved slowly in the experimental area and as such is an unusual ship noise source. The expected difference in travel time from this near-broadside location to SWAMI52 matches the short time EGF envelope peaks, as can be seen in Fig. 14(f). Thus, the high amplitude spurious signals in Fig. 13(a) are attributed to R/V *Oceanus*. The amplitude of the anomalous −0.0175 s peak in the EGF envelope of the summed normalized cross-correlations shown in the far right of Fig. 13(a) decreases to the background noise level when the period 12–24Z August 31 is excluded, as can be seen in Fig. 13(g).

Figures 13 and 14 suggest that the observation time period to obtain a stable EGF envelope depends on the distribution of the noise. Summing over September 2 yields a good approximation, as shown in Fig. 14(c), but summing over any of the other days or even summing over the entire 84 h period gives poorer results due to the increased proportion of directional bias of dominant events in the total received signal. Hence, when specific events dominate the

EGFs, either data from the times during which they occur should be discarded, or the cross-correlations need to be summed over an even longer period so that the effects of individual events are negligible. At any given time, except during the storm, the cross-correlation is generally dominated by one or two high amplitude events, and eliminating these from the data is difficult. For the case considered here with ship noise near the coast being a significant component of the noise field, the cross-correlations summed over many days or longer could show some directionality, corresponding to preferred shipping routes.

VII. CONCLUSION

Shallow water OAI in the ship dominated 20–100 Hz frequency band was considered using data from the Shallow Water 2006 experiment. Theory indicates that the time derivative of the cross-correlation yields an EGF, an approximation of an amplitude shaded Green's function. For an appropriate bandwidth, different time and frequency domain normalization methods yielded similar cross-correlation results. A major reason for this is the spatial averaging of the noise field, which occurs when noise from many ship tracks are recorded. Since ship noise is discrete, long cross-correlation periods were required to give sufficient averaging for the emergence of the Green's function. EGFs were here computed over 1 day, but shorter observation times could potentially be used. The EGFs are therefore average rather than instantaneous Green's functions.

Most ambient noise processing has focused on extracting the direct arrival, but the careful processing combined with the strong noise here allowed for extraction of higher order arrivals. Direct and surface-reflected paths between HLA hydrophones, as well as bottom-surface-reflected paths between HLA and VLA hydrophones, were determined from the EGF for three L-shaped arrays, in agreement with simulated travel times. The EGFs between equispaced HLA hydrophone pairs in a linear array are shown to have minimal variation. Analysis of temporal variations in the EGFs for horizontally propagating noise is generally dominated by one or two sources. The richer angular distribution of the breaking wave noise enabled construction of more vertically traveling paths. The EGFs obtained from data recorded during Tropical Storm Ernesto were clearer than those obtained before and after the storm.

The work here has focused on extracting high-quality arrivals from noise. These can potentially be used for array element localization,[6,36] ocean acoustic monitoring, and estimating sediment structure.

ACKNOWLEDGMENTS

Work supported by the Office of Naval Research under Grant No. N00014-05-1-0264, and by the Department of Energy National Energy Technology Laboratory via the Gulf of Mexico Hydrates Research Consortium, University of Mississippi. SWAMI data supplied by the Applied Research Laboratories, the University of Texas at Austin. Shark data supplied by Woods Hole Oceanographic Institute. L.A.B. is appreciative of support from a Fulbright Postgraduate Award in Science and Engineering, and from the Defence Science and Technology Organisation, Australia.

APPENDIX: TIME DOMAIN NORMALIZATION METHODS

This appendix outlines the mathematical details of three of the time domain normalization methods that were compared in Sec. IV D.

One-bit normalization, which uses only the sign of the signal, increases the signal-to-noise ratio of the data:

$$s_n(t) = \begin{cases} -1 & \text{if } s(t) < 0 \\ 1 & \text{if } s(t) > 0, \end{cases} \tag{A1}$$

where $s(t)$ is the raw signal at time t, and subscript n denotes the normalized signal.

RCTVW and ECTVW are the most computationally intensive time domain normalization techniques considered here. RCTVW normalizes each point by the sum of the unweighted mean of the absolute value of N preceding and succeeding values ($2N+1$ points overall):

$$s_n(t) = \frac{s(t)}{\omega(t)}, \tag{A2}$$

where

$$\omega(t) = \sum_{\tau=t-N}^{t+N} |s(\tau)| = \omega(t-1) - |s(t-N-1)| + |s(t+N)|. \tag{A3}$$

A normalization window of 0.05 s, the time interval of the maximum period, corresponding to the minimum frequency of 20 Hz, was found to be suitable. A normalization vector length of $2N+1=257$ was therefore used.

ECTVW places more emphasis on points closer to the point of interest. It normalizes in the same manner as RCTVW, the only difference being that it applies a weighting filter with an amplitude that decreases exponentially in both directions from the data point of interest:

$$\begin{aligned}\omega(t) &= (1-\alpha)^N |s(t-N)| + \cdots + (1-\alpha)|s(t-1)| + |s(t)| \\ &\quad + (1-\alpha)|s(t+1)| + \cdots + (1-\alpha)^N |s(t+N)|,\end{aligned} \tag{A4}$$

where $\alpha=2/(N+1)$ is the exponential smoothing factor. In order to use previously calculated sums to determine subsequent weights, the exponential is split up into two parts, the increasing exponential prior to and including the current point, and the decreasing exponential after the current point. These are then summed to give the overall weighting.

[1]O. I. Lobkis and R. L. Weaver, "On the emergence of the Green's function in the correlations of a diffuse field," J. Acoust. Soc. Am. **110**, 3011–3017 (2001).
[2]R. L. Weaver and O. I. Lobkis, "Ultrasonics without a source: Thermal fluctuation correlations at MHz frequencies," Phys. Rev. Lett. **87**, 134301 (2001).
[3]K. van Wijk, "On estimating the impulse response between receivers in a controlled ultrasonic experiment," Geophysics **71**, SI79–SI84 (2006).
[4]M. Campillo and A. Paul, "Long-range correlations in the diffuse seismic coda," Science **299**, 547–549 (2003).
[5]R. Snieder, "Extracting the Green's function from the correlation of coda

waves: A derivation based on stationary phase," Phys. Rev. E **69**, 046610 (2004).
[6]N. M. Shapiro, M. Campillo, L. Stehly, and M. H. Ritzwoller, "High-resolution surface-wave tomography from ambient seismic noise," Science **307**, 1615–1618 (2005).
[7]K. G. Sabra, P. Gerstoft, P. Roux, W. A. Kuperman, and M. C. Fehler, "Surface wave tomography from microseisms in Southern California," Geophys. Res. Lett. **32**, L14311 (2005).
[8]K. G. Sabra, P. Gerstoft, P. Roux, and W. A. Kuperman, "Extracting time-domain Green's function estimates from ambient seismic noise," Geophys. Res. Lett. **32**, L03310 (2005).
[9]K. Wapenaar and J. Fokkema, "Green's function representations for seismic interferometry," Geophysics **71**, SI33–SI46 (2006).
[10]E. Larose, A. Khan, Y. Nakamura, and M. Campillo, "Lunar subsurface investigated from correlation of seismic noise," Geophys. Res. Lett. **32**, L16201 (2005).
[11]A. Curtis, P. Gerstoft, H. Sato, R. Snieder, and K. Wapenaar, "Seismic interferometry-turning noise into signal," The Leading Edge **25**, 1082–1092 (2006).
[12]G. D. Bensen, M. H. Ritzwoller, M. P. Barmin, A. L. Levshin, F. Lin, M. P. Moschetti, N. M. Shapiro, and Y. Yang, "Processing seismic ambient noise data to obtain reliable broad-band surface wave dispersion measurements," Geophys. J. Int. **169**, 1239–1260 (2007).
[13]P. Roux and M. Fink, "Green's function estimation using secondary sources in a shallow water environment," J. Acoust. Soc. Am. **113**, 1406–1416 (2003).
[14]P. Roux, W. A. Kuperman, and the NPAL Group, "Extracting coherent wave fronts from acoustic ambient noise in the ocean," J. Acoust. Soc. Am. **116**, 1995–2003 (2004).
[15]K. G. Sabra, P. Roux, and W. A. Kuperman, "Arrival-time structure of the time-averaged ambient noise cross-correlation function in an oceanic waveguide," J. Acoust. Soc. Am. **117**, 164–174 (2005).
[16]K. G. Sabra, P. Roux, A. M. Thode, G. D'Spain, W. S. Hodgkiss, and W. A. Kuperman, "Using ocean ambient noise for array self-localization and self-synchronization," IEEE J. Ocean. Eng. **30**, 338–347 (2005).
[17]M. Siderius, C. H. Harrison, and M. B. Porter, "A passive fathometer technique for imaging seabed layering using ambient noise," J. Acoust. Soc. Am. **120**, 1315–1323 (2006).
[18]L. A. Brooks and P. Gerstoft, "Ocean acoustic interferometry," J. Acoust. Soc. Am. **121**, 3377–3385 (2007).
[19]P. Gerstoft, W. S. Hodgkiss, M. Siderius, C.-F. Huang, and C. H. Harrison, "Passive fathometer processing," J. Acoust. Soc. Am. **123**, 1297–1305 (2008).
[20]C. H. Harrison and M. Siderius, "Bottom profiling by correlating beam-steered noise sequences," J. Acoust. Soc. Am. **123**, 1282–1296 (2008).
[21]P. Roux, K. G. Sabra, W. A. Kuperman, and A. Roux, "Ambient noise cross correlation in free space: Theoretical approach," J. Acoust. Soc. Am. **117**, 79–84 (2005).
[22]K. Wapenaar, "Green's function retrieval by cross-correlation in case of one-sided illumination," Geophys. Res. Lett. **33**, L19304 (2006).
[23]J. Traer, P. Gerstoft, P. D. Bromirski, W. S. Hodgkiss, and L. A. Brooks, "Shallow-water seismoacoustic noise generated by tropical storms Ernesto and Florence," J. Acoust. Soc. Am. **124**, EL170–EL176 (2008).
[24]R. J. Urick, *Principles of Underwater Sound* (McGraw-Hill, New York, 1975).
[25]R. Snieder, K. Wapenaar, and K. Larner, "Spurious multiples in seismic interferometry of primaries," Geophysics **71**, SI111–SI124 (2006).
[26]C. M. Bender and S. A. Orszag, *Advanced Mathematical Methods for Scientists and Engineers: Asymptotic Methods and Perturbation Theory* (McGraw-Hill, New York, 1978).
[27]A. Derode, E. Larose, M. Tanter, J. de Rosny, A. Tourin, M. Campillo, and M. Fink, "Recovering the Green's function from field-field correlations in an open scattering medium," J. Acoust. Soc. Am. **113**, 2973–2976 (2003).
[28]N. Harmon, P. Gerstoft, C. A. Rychert, G. A. Abers, and K. M. Fischer, "Phase velocities from seismic noise using beamforming and cross correlation in Costa Rica and Nicaragua," Geophys. Res. Lett. **35**, L19303 (2008).
[29]S. E. Fried, W. A. Kuperman, K. G. Sabra, and P. Roux, "Extracting the local Green's function on a horizontal array from ambient ocean noise," J. Acoust. Soc. Am. **124**, EL183–EL188 (2008).
[30]P. Gerstoft, K. G. Sabra, P. Roux, W. A. Kuperman, and M. C. Fehler, "Green's functions extraction and surface-wave tomography from microseisms in southern California," Geophysics **71**, SI23–SI31 (2006).
[31]H. Schmidt, *OASES Version 3.1 User Guide and Reference Manual*, Department of Ocean Engineering, Massachusetts Institute of Technology, 2004.
[32]A. Derode, A. Tourin, and M. Fink, "Ultrasonic pulse compression with one-bit time reversal through multiple scattering," J. Appl. Phys. **85**, 6343–6352 (1999).
[33]E. Larose, A. Derode, M. Campillo, and M. Fink, "Imaging from one-bit correlations of wideband diffuse wavefields," J. Appl. Phys. **95**, 8393–8399 (2004).
[34]Y. Yang, M. H. Ritzwoller, A. L. Levshin, and N. M. Shapiro, "Ambient noise Rayleigh wave tomography across Europe," Geophys. J. Int. **168**, 259–274 (2007).
[35]J. A. Goff, B. J. Kraft, L. A. Mayer, S. G. Schock, C. K. Sommerfield, H. C. Olson, S. P. S. Gulick, and S. Nordfjord, "Seabed characterization on the New Jersey middle and outer shelf: Correlatability and spatial variability of seafloor sediment properties," Mar. Geol. **209**, 147–172 (2004).
[36]L. A. Brooks, P. Gerstoft, and D. P. Knobles, "Multichannel array diagnosis using noise cross-correlation," J. Acoust. Soc. Am. **124**, EL203–EL209 (2008).